Journal of
Materials Chemistry C

Materials for optical, magnetic and electronic devices

Accepted Manuscript

This article can be cited before page numbers have been issued, to do this please use: L. D. Rosales-Vazquez, J. Valdes-García, J. M. German-Acacio, J. C. Páez-Franco, D. Martínez-Otero, A. R. Vilchis-Néstor, J. Barroso-Flores, V. Sanchez-Mendieta and A. Dorazco-González, *J. Mater. Chem. C*, 2022, DOI: 10.1039/D2TC00291D.

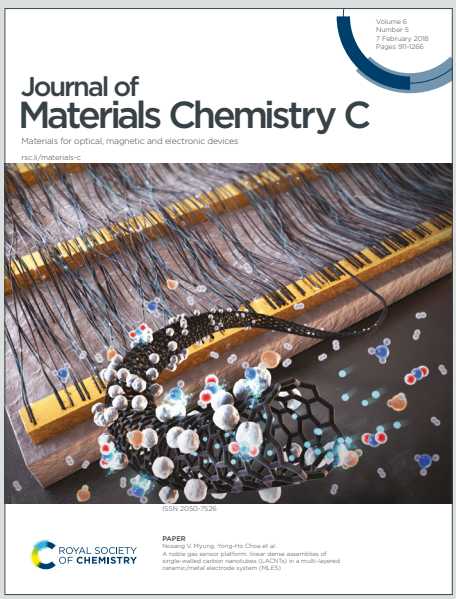

ROYAL SOCIETY OF CHEMISTRY

rsc.li/materials-c

View Article Online
DOI: 10.1039/D2TC00291D

ARTICLE

A Water-Stable Luminescent Zn-MOF Based on a Conjugated π-electron Ligand as an Efficient Sensor for Atorvastatin and Its Application in Pharmaceutical Samples

Received 00th January 20xx,
Accepted 00th January 20xx

DOI: 10.1039/x0xx00000x

Luis D. Rosales-Vázquez,[a] Josue Valdes-García,[a] J. M. Germán-Acacio,[b] José C. Páez-Franco,[b] Diego Martínez-Otero,[c] Alfredo R. Vilchis-Néstor, Joaquín Barroso-Flores,[c] Víctor Sánchez-Mendieta[c*] and Alejandro Dorazco-González[a*]

Atorvastatin is amongst the most worldwide-prescribed drugs for cholesterol-lowering treatment. In this work, a novel water-stable 3D porous metal-organic framework $\{[Zn_3(Htptc)_2]\cdot(H_2O)_{1.3}\cdot(CH_3CH_2OH)_{3.1}\}_n$, **1** ($H_4$tptc= terphenyl-3,3”,5,5”-tetracarboxylic acid) was synthesized, structurally determined by single-crystal X-ray diffraction, and studied in-depth as a luminescent sensor for a series of statins and common biological ions (oxyanions, dicarboxylates, citrate, and adenosine 5’-triphosphate) in 20% aqueous ethanol. The luminescence of **1** can be effectively quenched by atorvastatin (K_{SV}= 1.40 x 10^5 M^{-1}) with a pronounced selectivity over other typical statins such as fluvastatin, pravastatin, and rosuvastatin. The efficient quenching response exhibits excellent selectivity even in the presence of coexisting species in blood plasma and urine with a detection limit of 4.2 µmol L^{-1}. On the basis of multiple spectroscopic tools (fluorescence, UV-Vis, powder X-ray diffraction, lifetimes), the crystal structure of **1**, SEM observations, EDS analysis, and DFT calculations, the sensing mechanism is proposed via a static-complexation PET process driven through π-stacking interactions between π–electron-rich terphenyl ligand and two aromatic rings from the atorvastatin. Neutral aqueous-phase dispersions of **1** allow for the detection of atorvastatin in real pharmaceutical samples.The utilization of MOFs-based materials as luminescent sensors for selective and sensitive detection of atorvastatin has not been explored till now.

1. Introduction

Luminescent metal-organic frameworks (LMOFs) are light-emitting crystalline solids based on supramolecular complexes with a fascinating structural diversity, typically, these materials are constructed by the combination of fluorescent multidentate linkers and diamagnetic or lanthanide metal centers.[1-8] Of particular interest are porous d^{10} transition-metal LMOFs containing conjugated π-electron multicarboxylate ligands owing to their functionality as host matrix materials,[9-11] light-emitting devices,[12-14] materials for gas adsorption/separation,[15-17] catalysis,[18-20] and as receptors of small molecules.[21-22] Generally, d^{10} metal LMOFs with accessible pore volumes undergo a guest binding-induced fast photoluminescence change.[1,12,23-28]

Reports in the context of reticular chemistry have shown that Zn-MOFs constructed with terphenyl-tetracarboxylic acid (H_4tptc) generate crystalline networks based on a $[Zn_2(COO)_4]$ complex as paddlewheel secondary building unit (SBUs). These materials are blue/green luminescent and possess well-defined nanoporous[12,16-17] or 1D channels[14,29-33] where the solvent accessible volume is > 20% of the total volume.[32]

Up to now, luminescent Zn-MOFs constructed with derivatives of π-electron-rich terphenyl-carboxylate ligand have proven to be useful in the quantitative detection of inorganic ions,[31] explosive nitroaromatic compounds,[14,30,32-35] and pesticides.[4,36-37] However, optical detection of drugs with global relevance such as statins practically remains unexplored.

Statins are among the most used drugs worldwide for decreasing blood cholesterol and cardiovascular medication.[38-39] Heart diseases are the leading cause of death worldwide and commonly, are the result of coronary atherosclerosis. A central factor of atherosclerosis is the accumulation of cholesterol in arterial walls, making lipid modification critical to heart diseases prevention.[40]

The most used cholesterol-lowering statins in medical purposes include sodium or calcium salts of atorvastatin, fluvastatin, pravastatin, and rosuvastatin (**Fig. 1**).[38] Among these drugs, atorvastatin is one of the oldest and worldwide-prescribed because it has shown the highest lipoprotein cholesterol lowering efficacy in humans at a maximum daily dose ≈ 80 mg.[41]

Common analytic methods for the quantitative detection of atorvastatin include electrochemical sensors,[42-45] Raman

[a] Instituto de Química, Universidad Nacional Autónoma de México. Circuito Exterior, Ciudad Universitaria, Ciudad de México, 04510, México. E-mail: adg@unam.mx
[b] Red de Apoyo a la Investigación, Instituto Nacional de Ciencias Médicas y Nutrición SZ-Universidad Nacional Autónoma de México (CIC-UNAM)
[c] Centro Conjunto de Investigación en Química Sustentable UAEM-UNAM, Carretera Toluca-Ixtlahuaca Km. 14.5, San Cayetano, Toluca, Estado de México, 50200, México. E-mail: vsanchezm@uaemex.mx

†Electronic Supplementary Information (ESI) available: [details of any supplementary information available should be included here]. See DOI: 10.1039/x0xx00000x

View Article Online
DOI: 10.1039/D2TC00291D

ARTICLE

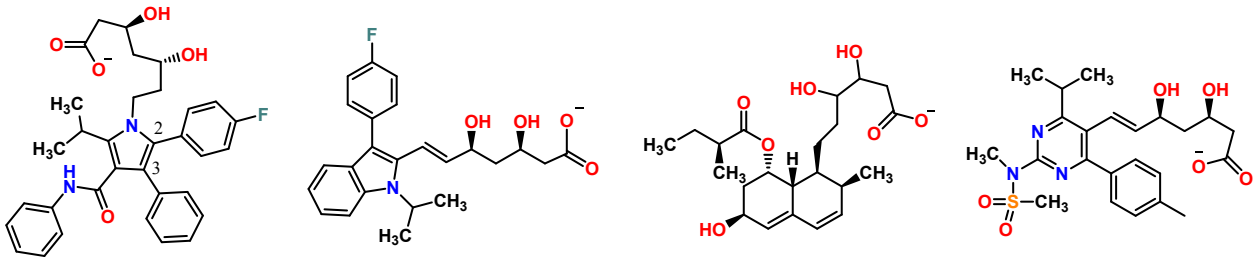

Fig. 1. Statins used as analytes in this study. Sodium salts for FLV/PRV and calcium salts for ATV/RSV.

spectroscopy,[46-48] electrophoresis,[38] spectrophotometry[49] and chromatographic-mass spectrometry.[38,41,50-55] However, many of these methods require considerable setup, analysis time and/or high-cost instruments. While the need for direct, and timely selective sensors for atorvastatin, capable of operating in real samples is evident, so far, a very limited number of systems have been described which are based on carbon nanotubes functionalized with polypyrrole films,[44] Fe_3O_4-nanoparticles,[42] Au-nanoparticles,[56] graphene,[57] and zinc oxide[58] or by oxidative coupling reactions with Ce(IV)-complexes.[59]

Frequently, these electrochemical nanosensors show limits of detection between 10^{-4} and, 10^{-9} M, and their sensing mechanisms are based on the electro-oxidation reaction of the pyrrole ring[57,60] or oxidative reaction of aromatic fragments.[59] Consequently, they are not particularly selective and interferences from other statins containing these rings such as fluvastatin or pravastatin can be a problem.

Reports in the field of sorbent materials have shown that the porous Zn(II)-zeolite imidazolate framework-8 (ZIF-8) is able to capture atorvastatin directly from urine.[61] However, the creation of a potent and selective luminescent sensor/receptor for atorvastatin is an ongoing challenge.

Taking the highly π-electron-rich density, porosity, and strong luminescent of d^{10}-MOFs with terphenyl derivatives, into account we surmised that a sensitive atorvastatin sensor can be achieved by a water-stable Zn-LMOF derivative of terphenyl-tetracarboxylate where the selectivity can be driven through π-π stacking between π-electron-rich surface of the ligand and the fluorinated aromatic π-electron-deficient ring from atorvastatin.[62]

With the objective of constructing the first example of a metal-organic framework-based sensor for atorvastatin, we have prepared a new luminescent Zn-MOF, **1** with selective performance for atorvastatin sensing in aqueous media and pharmaceutical samples. The results obtained for this system including synthesis, crystal structure, multiple spectroscopic sensing studies, SEM-EDS characterization, and theoretical DFT calculations are summarized below.

2. Results and Discussion

2.1 Structural description and characterization

By solvothermal method, the LMOF $\{[Zn_3(Htptc)_2]\cdot(H_2O)_{1.3}\cdot(CH_3CH_2OH)_{3.1}\}_n$, **1** was synthesized through the reaction of $Zn(OTf)_2$ with H_4tptc ligand in DMF-ethanol-water (v/v, 8/2/2) (**Fig. 2A**). Single-crystal X-ray diffraction reveals that crystallized in a monoclinic *C2/c* space group (**Table S1**). There are two crystallographically independent Zn(II) ions, each one is coordinated by six oxygen atoms forming a distorted octahedral geometry (**Fig. 2B**). The carboxylate oxygen atoms of two Htptc ligands link the three Zn(II) ions, generating thus trinuclear SBUs (**Fig. 2C,** for schematic SBU see **Fig. S1**). The Zn-O bond lengths range from 1.996(5) to 2.428(6) Å (**Table S2**).

Zn(II)-based MOFs with $tptc^{4-}$ ligand have recently been described having paddlewheel dinuclear SBUs and different topologies; $\{[Zn_2(tptc)(aminopyridine)_x(H_2O)]\cdot H_2O\}_n$ with a **NbO** net,[32] $\{[Zn_2(tptc)(DMF)_3]\cdot(H_2O)_4\cdot(DMF)_{5.5}\}_n$ and $\{[Zn_2(tptc)(DMA)(H_2O)]\cdot(H_2O)\cdot(DMA)_{3.5}\}_n$ (DMA= dimetilacetamide) with **dia** an **lon** nets, respectively.[35] Due to the combining chelate bidentate, bridging monodentate and oxo-bridging coordination modes of the carboxylate oxygen atoms of $Htptc^{-3}$ in **1**, each SBU is bridged by eight Htptc ligands (**Fig. 2C**) and each ligand is linked to four trinuclear clusters, which results in a three-dimensional framework (**Fig. 2C**). The network topology of **1** was studied by software package TOPOS-PRO, which consists of a new underlying 4,6,7-c net and a new 3,3,8-c net in standard and cluster representations of valence-bonded MOFs, respectively (**Fig. 2D** and **Fig. S2**).[63]

In this assembly, there are connected oval-shape pores along *a*-axis as shown in **Fig. 3** and **Fig. S3**. SQUEEZE/PLATON calculations[64] yield a solvent accessible volume of 33.5 % of the total volume; this is, 1886 $Å^3$ out of 5301.0 $Å^3$ per unit cell volume. Further studies of voids in **1** were performed using the Mercury software,[65] which provided a representation of the free volume available in the crystalline structure of **1** (**Fig. 3** and **Fig. S4**). The free volume is extended through the array;

View Article Online
DOI: 10.1039/D2TC00291D

ARTICLE

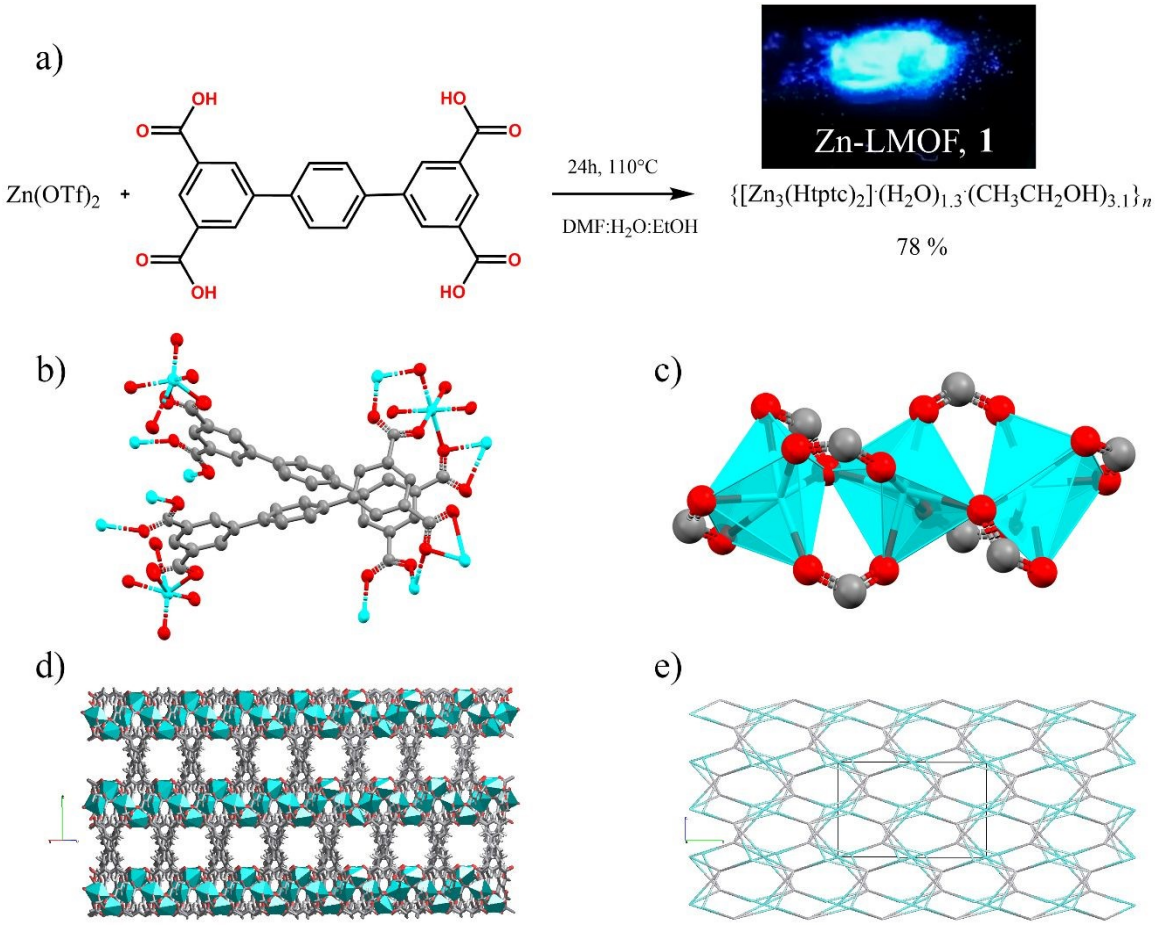

Fig. 2. a) Synthesis path for **1**. Inset: **1** under irradiation at 365 nm UV illumination. b) Molecular structure of **1** (hydrogen atoms and lattice molecules are omitted for clarity; ellipsoids shown at 50% probability). c) Trinuclear SBU of **1**. d) 3-D framework of **1** (solvent molecules are omitted for clarity). e) Simplified topology network of **1**.

although the irregular channels seem small, they lead to larger voids that have the peculiarity of having carboxylic oxygen atoms exposed along the walls of these cavities.

Comparison of the experimental powder X-ray diffraction (PXRD) patterns with those calculated from the crystal structure of the as-synthesized **1** match well regarding to positions and the relative intensities of the peaks (**Fig. 3B**), confirming high phase purity, thus, this sample was used for further experiments.

Elemental analysis (C, N, H) was consistent with the composition of a single crystal of **1**. Next, the chemical stability of **1** in an aqueous medium was carried out by PXRD and IR-ATR. The main diffraction peaks of **1** in the range from 5 to 27°after immersion in an aqueous solution containing 50% ethanol at room temperature for 24 h are in good agreement with the starting compound Zn-LMOF **1** as is depicted in **Fig. 3B**. The water stability of **1** was also confirmed by FTIR-ATR spectroscopy (**Fig. S5**).

The thermal analyses of **1** were measured in the temperature range from 25 to 450 °C (**Fig. S6**), with a heating rate of 10 °C per min under a N_2 atmosphere. The TGA profile shows a weight loss of a calculated 13.28 % during the 120-297°C interval which can be ascribed to the loss of 3.1 molecules of ethanol and one water molecule. The percentage is congruent with the estimated theoretical expected weight loss from the solvent molecules (13.73 %).

The solid-state ^{13}C cross-polarization/magic angle–spinning NMR spectrum of **1** (**Fig. S7**) is consistent with the asymmetric unit of the crystal structure and supports the purity of **1**. The spectrum shows four expected signals for the four crystallographically independent atoms of -CO_2 in the range of 170 - 178 ppm. Similar solid-state ^{13}C-atoms chemical shifts have been observed with Zn-coordination polymers and Zn-MOFs based on benzene-dicarboxylates.[66] The six signals located in the range 138 – 150 ppm can be ascribed to the

View Article Online
DOI: 10.1039/D2TC00291D

ARTICLE

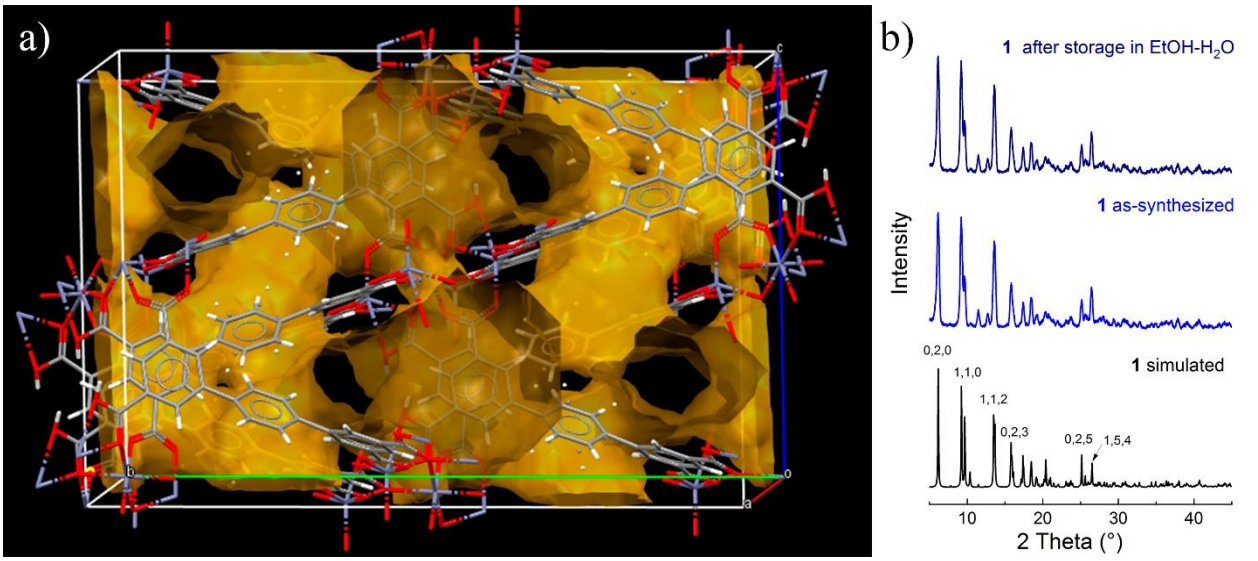

Fig. 3. a) Depiction of void surfaces for a packing section of **1**. Atom codes: Zn (blue), C (grey), O (red) and H (white). b). Simulated (bottom) and experimental powder X-ray diffraction patterns of **1** before (middle) and after (top) storage in aqueous media for 24 hours.

$^{13}C_{quaternary}$ atoms[67] and, the intense and broad signals between 128 and 137 ppm can be assigned to aromatic ^{13}CH atoms.[6]

In general, all peaks of the aromatic ^{13}CH atoms are broad and are not fully resolved, which makes their assignment difficult. From the crystal structure of **1,** the central phenyl ring presents a rotational disorder that causes the signals to widen (**Fig. S8**).[67]

Solvent-free form of **1** was successfully obtained by heating at 90 °C under vacuum for 2 h. Comparison of the PXRD patterns of **1** and its solvent-free form is in agreement with regard to both positions and the relative intensities of the peaks indicating good framework stability (**Fig. S9**). This fact is not unexpected due to the structural rigidity of **1** and the weak interaction with solvent molecules observed in its crystal structure.

The TGA curve (**Fig. S10**) shows no obvious weight loss between 25 and 310 °C which confirms the absence of the lattice solvents in **1**.

2.2 Luminescence study and sensing of statins

The luminescence spectra of **1** and free ligand (H_4tptc) in the solid-state were examined at room temperature (**Fig. S11**). Upon excitation at 330 nm, **1** displays an enhanced blue emission peak at 430 nm in comparison to free ligand with an emission peak at 465 nm. This blue emission enhancement (≈ 34 nm) can be assigned mainly to ligand-centered electronic transitions (IL) perturbed by the coordination of the π-conjugated ligand to the Zn(II) ions.[35] The fluorescence intensity enhancement of **1** can be assigned to the increase of the rigidity of the ligand in the final crystal arrangement, which reduces the loss of energy through non-radiative relaxation processes.[68-69]

On the other hand, aqueous dispersions of **1**, containing 80 vol. % ethanol, are blue-emitting mixtures with a maximum at 440 nm (λ_{ex}= 330 nm). The quantum yield (Φ_{PL}) of the aqueous dispersion of **1** is 32.51%, this value is higher compared to the free ligand in ethanol-water ($\Phi_{PL(H4tptc)}$= 14.25 %).[70]

The emission spectra of the ethanol-water dispersions of **1** (20 μM) at pH= 7.0 before and after 24 h show no obvious changes in luminescent intensities compared to the original spectrum, indicating high stability. Thus, those conditions were used for further studies.

Taking the π-electron-rich fragment, porosity, water-stability, and luminescent performance of **1**, into account, we studied its utility as an optical sensor towards statins containing fluorinated π-electron-deficient rings such as ATV and FLV, additionally, other statins lacking those fluorinated aromatic rings were investigated for comparison purposes. To quantitatively sense the calcium salt of ATV, a fluorescent titration experiment was carried in ethanol-water (v/v, 8/2) at neutral pH. As shown in **Fig. 4A,** an efficient quenching response (87%) of the aqueous dispersion of **1** occurs upon the incremental addition of ATV in a micromolar concentration range. The quenching effect can be quantitatively analyzed by the linear Stern–Volmer (S-V) equation (1).

$$\frac{I_0}{I} = (1 + K_{SV}[analyte]) \qquad Eq.\ (1)$$

View Article Online
DOI: 10.1039/D2TC00291D

ARTICLE

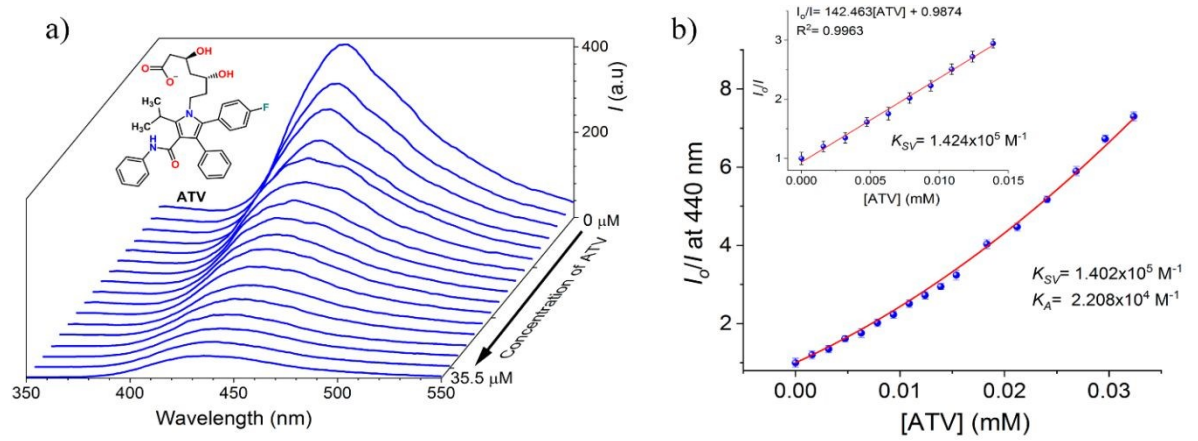

Fig. 4. a) Emission spectra (λ_{ex}= 330 nm) of **1** dispersed in ethanol-water (v/v, 8/2) at pH= 7.0 upon additions of increasing amounts of ATV calcium. b) S-V plot at 440 nm, the solid line was obtained by fitting to Eq. (2). Inset: Solid line was obtained by fitting to linear S-V Eq. (1).

where K_{SV} (M^{-1}) is the quenching constant, I_o and I are the luminescent intensities before and after the addition of the analyte and [analyte] is the molar concentration of the target species. **Fig. 4B** shows the S-V plot at 440 nm (λ_{ex}= 330 nm) with increasing ATV concentration up to 35 μM. Notably, there was a linear dependence of the luminescence intensity on the ATV concentration in the range of 0 - 16 μM (Inset, **Fig. 4B**). This linear data can be well fitted to I_o/I= 0.987 + 142.466[ATV], with a correlation coefficient (R^2= 0.9963).

In addition, the complete profile at higher concentration shows a clear upward curvature, which is typically observed when static quenching contributes to the effect involving a specific binding between the receptor and the analyte.[71]The profile at high concentrations can be well fitted to the theoretical equation (2) proposed by Fabbrizzi *et al.*,[72] (**Fig. 4B**), which considers a simultaneous dynamic and static quenching process when the ground state complexation quenches the emission completely and the receptor-analyte complex practically does not emit.

$$\frac{I_0}{I} = (1 + K_{SV}[analyte])(1 + K_A[analyte]) \qquad Eq.\ (2)$$

In this expression, K_{SV} and K_A correspond to quenching (dynamic process) and apparent binding (static process) constants, respectively. K_{SV} value of **1** by the addition of ATV is 1.402(±0.11) x 10^5 M^{-1}. The value of K_{SV} is consistent both in the

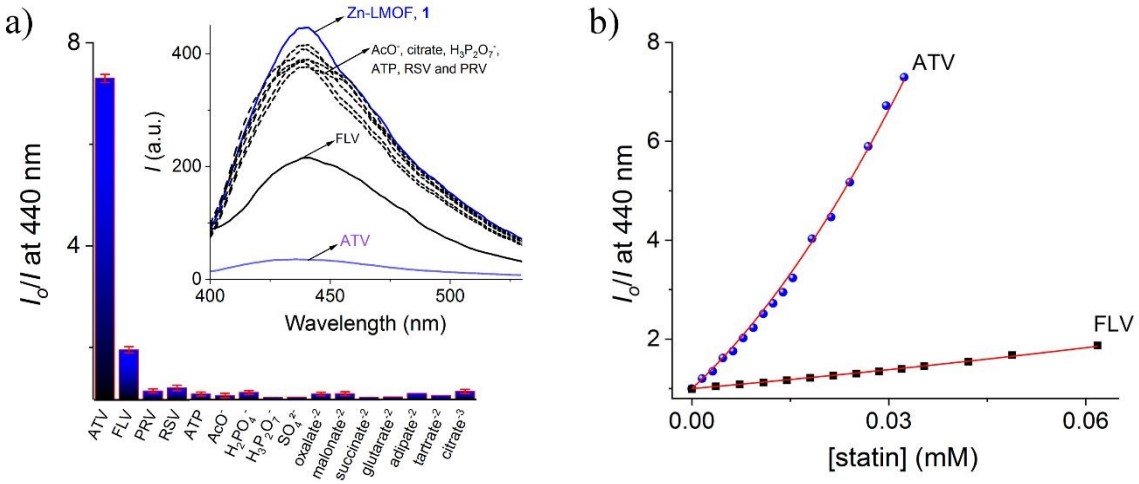

Fig. 5. a) Relative emission intensities at 440 nm of ethanol-water (v/v, 8/2) dispersion of **1** upon additions of different anions ($[X]_{final}$= 100 μM). Inset: The corresponding luminescence spectra (λ_{ex} = 330 nm) at 25 °C. In all measurements, the ionic strength was adjusted to 50 mM of NaCl. b) Profiles of emission titration experiments at 440 nm of **1** by ATV (0 - 35 μM) and FLV (0 - 62 μM). The solid lines were obtained by fitting the data to the Eq. (2).

View Article Online
DOI: 10.1039/D2TC00291D

ARTICLE

linear fit at low concentrations (≤ 16 μM) and, at high concentrations. The *apparent* binding constant was estimated with a value of K_A= 2.208(±0.13) x 10^4 M^{-1}, this finding is interesting because suggests a binding-induced quenching partial process between **1** and ATV.

The detection limit (LOD) of **1** towards ATV was calculated by the equation 3σ/*S*,[47] where σ is the standard deviation of luminescent intensity of blank for ten times and *S* is the slope (K_{SV}) of the calibration curve obtained from concentration-dependent luminescence intensity profile at 440 nm (Inset: **Fig. 4B**). LOD was estimated to be 4.21 μM.

As is shown in **Table S3**, the LOD of **1** is comparable to other recent electrochemical and chromogenic sensors reported in the literature.[42,44,56-60,73-74] Next, the anion selectivity of **1** was analyzed. Salts of an extensive series of anions including FLV, PRV, RSV, inorganic oxyanions, organic (di)carboxylates, citrate and ATP ($[X]_{final}$= 200 μM) were added to a buffered ethanol-water dispersion of **1**, and the emission intensity at 440 nm was recorded. All oxyanions, carboxylates, PRV, and RSV gave a very low response, **Fig. 5A.** The addition of FLV resulted in a modest quenching in emission intensity, but it was still significantly lower than that observed for ATV. The quenching fluorescence parameters with FLV were also determined by a titration experiment under the same conditions as in **Fig. S12**.

The S-V profile of FLV showed also slight upward curvature at high concentrations, the fitting using Eq. (2) afforded a quenching constant of 2 orders of magnitude lower than for ATV (K_{SV}(FLV)= 6.68(±0.08) x 10^3 M^{-1}). The S-V profiles for both statins are shown in **Fig. 5B**.

2.3 Selective and sensing performance for ATV

For practical applications, luminescent statin-sensors are required to have not only a good optical response but also selectivity in the presence of coexistent potential interferences in physiological samples.[75] Therefore, a selectivity experiment of **1** toward common interfering species in blood plasma and urine, such as D-glucose, creatinine, urea, L-proline, ATP, NaCl, KCl, NH_4Cl, $MgCl_2$, and HCO_3^-, was carried out at neutral pH.

Addition of these species to an aqueous dispersion of **1** induced a negligible change of its emission as shown in **Figs. 6A-B. Fig. 6D** shows that the quenching response at 440 nm generated by ATV (I_o/I≈ 7.5) is not affected by the background ingredients of the common blood plasma and urine demonstrating thus selectivity performance.

As a result, only ATV induces a strong quenching with color change from blue to colorless under UV light (**Fig. 6C**). This indicates that **1** can act as a visual sensor for recognizing ATV in aqueous media. Undoubtedly **1** can potentially act as a selective luminescent sensor for ATV in presence of interfering species components of urine and blood plasma even in pharmaceutical samples; however, the presence of other components with a blue emission, specifically, in real blood plasma as proteins or tryptophan derivatives could elicit an

View Article Online
DOI: 10.1039/D2TC00291D

ARTICLE

Table 1. Results of the luminescent sensing method of ATV calcium in pharmaceutical samples using **1** and HPLC-UV method.

Sample	ATV labeled (mg/table)	ATV found by luminescence using **1** (mg/tablet)[a]	Recovery (%) ± RSD (%)[b]	ATV found by HPLC-UV method
Eturion 20	20.00	18.86	94.03 ± 2.3	18.98
Sortis 20	20.00	19.34	96.70 ± 1.5	19.17

[a] Average of three measurements

interference. The reusability of **1** by removal of ATV was investigated. After the detection experiments, **1** was immersed in 10 ml of ethanol-DMF (v/v, 9:1) for **1** h at 40°C. Then, the structural stability and emission properties were monitored by PXRD and fluorescence spectroscopy. In general, the intensity of blue-luminescence of **1** could only be recovered to 94% after the first run and decreased steadily during 4 cycles to 76 % (**Fig. S13**) but could still be fully quenched by the addition of ATV ([X]= 100 μM) in each cycle. PXRD pattern of **1** after 4 cycles was practically the same to that of the starting material, indicating that structure was preserved (**Fig. S14**).

2.4 Determination of ATV in pharmaceutical samples

To probe the utility of **1**, we have determined the ATV concentration in pharmaceutical samples. ATV calcium salt extraction and purification from commercial tablets were carried out as described below.[56]

A table of the corresponding pharmaceutical product containing ATV calcium (Eturion 20 or Sortin 20, both from Pfizer) was triturated, and dissolved in warm ethanol. After ultrasonication for 20 min., the resulting mixture was filtered, and effluent was collected. Then, the solvent was evaporated until dryness, obtaining solid white powder corresponding to ATV, which was characterized by FTIR-ATR spectroscopy and used to prepare a stock solution in 50 mL of ethanol. For the luminescent detection, a portion of this stock solution (50 μL) was added to 1950 μL of an ethanol-water (v/v, 8/2) dispersion of **1** (20 μM) containing 50 mM of NaCl and 10 mM MOPS (pH= 7.0), and the emission intensity at 440 nm was recorded (**Fig. S15**). The ATV concentration was then calculated using the fitting equation derived from the S-V plot experiment (Inset **Fig. 4B**). A comparison between reported and determined ATV

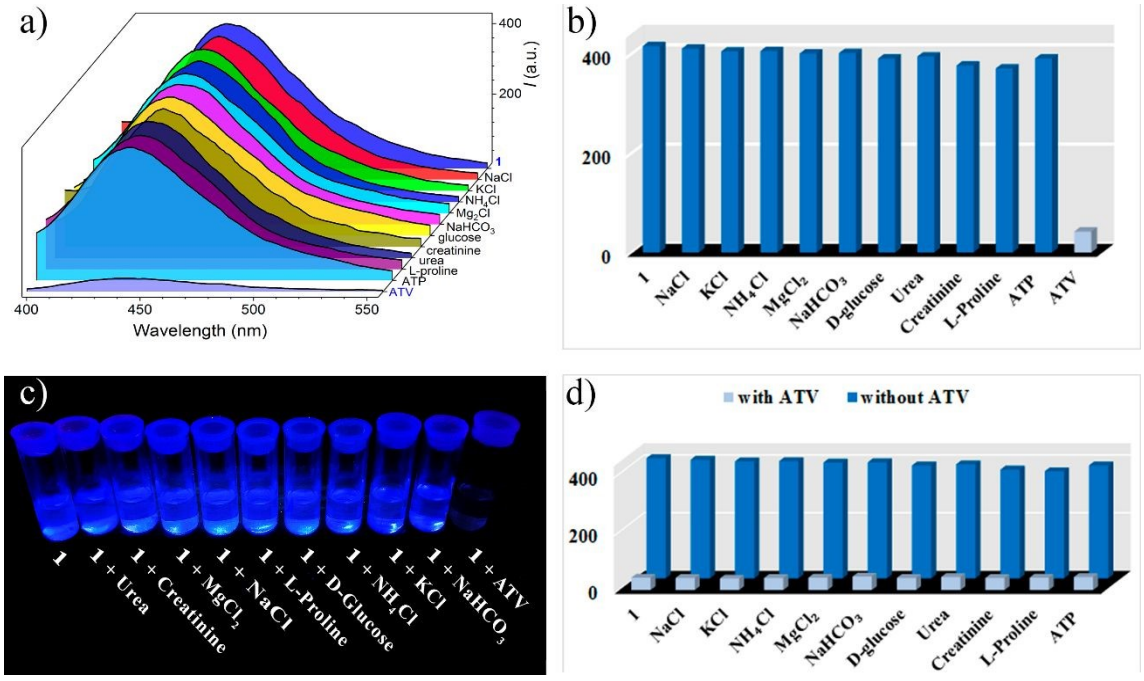

Fig. 6. a) Luminescence spectra. b) Intensities at 440 nm of ethanol-water dispersions of **1** at pH = 7.0 with several blood plasma and urine components. c) the corresponding photographs under UV light at 254 nm. d) luminescence responses of **1** towards ATV in the presence of a background of several blood plasma and urine species, 1.0 mM (bottom).

View Article Online
DOI: 10.1039/D2TC00291D

concentrations is given in **Table 1**. The percentage recoveries were obtained ranging from 94.03 to 96.70 %, and the relative standard deviations (RSD) were less than 2.3 % which indicated the proposed sensor could be used to analyze ATV in real pharmaceutical samples. The luminescent method with **1** was validated by an HPLC-UV quantification (**Fig. S16**).

2.5 Recognition mechanism investigation

The recognition mechanism of ATV by **1** was investigated by spectroscopic tools, electron microscopy and DFT calculations. The first evidence of the interaction process was obtained by UV-Vis spectrophotometry measurements. Crystals of **1** (10 mg) were immersed in 20 mL of an ethanolic solution of ATV (100 μM). Then, an aliquot (350 μL) of this solution was added to a cell containing 2500 μL of ethanol and the absorbance was recorded. The amount of this statin in the supernatant was measured using the characteristic absorbance at 247 nm (log ε= 4.674) over a period of 7 h. The results are plotted in **Fig. 7A-B**, these clearly show a continuous decrease of the amount of ATV in the supernatant, and this fact strongly suggests capture or strong interaction process between MOF and the statin. The quantity of recognized/captured ATV at the equilibrium was computed using the following equation (3).[76]

$$Q_{eq} = \frac{(C_o - C_{eq})V}{m} \qquad Eq.\ (3)$$

where Q_{eq} is the amount of ATV captured by **1**, (expressed in mmol g^{-1}), C_0 is the initial concentration of ATV (in mmol L^{-1}), C_{eq} (mmol L^{-1}) is the concentration of ATV at the equilibrium, V (L) is the volume of ATV solution and m is the mass of crystals that we soaked (given in grams). By calculations the value of Q_{eq} for recognized/captured ATV was 0.193 mmol g^{-1}.

Next, FTIR-ATR spectrum and PXRD pattern of **1** soaked in a water-ethanol concentrated solution of ATV for 24 h were recorded. IR spectrum and the PXRD pattern of **1** treated with ATV were very similar to that of the starting material, indicating that the Zn-LMOF structure was preserved (**Fig. S17-S18**). Therefore, the luminescence quenching is not due to the structural decomposition of **1**.

To study the fluorescence quenching process, the fluorescence lifetimes of **1** before and after the addition of concentrate solution of ATV were measured. An ethanol-water dispersion of **1** upon excitation with a 354 nm laser displayed a biexponential decay with values of $\tau_1 = 7.80$ and $\tau_2 = 1.46$ μs (**Fig. 7B**). Similar photophysical properties and values of luminescence lifetime have been previously reported for a structurally related MOF, $[Zn_2(tptc)(apy)_2(H_2O)_x]\cdot H_2O$ (apy= aminopyridine) where the microsecond time-scale luminescence is mainly attributed to singlet and triplet states from the organic linker tptc.[32]

The lifetime of **1** after the addition of a concentrated solution of ATV has a negligible change, in comparison with original aqueous suspension, confirming that a static quenching is dominant in the quenching mechanism.[77]

SEM images of **1** are shown in **Fig. S19A**, a crystalline material with well-defined facets, edges and ends can be observed, higher magnification micrographs revels flower-like morphology formed from crystals assembly of individual MOF's.

In contrast, **1** after the contact with ATV is evident that the morphology is altered, from triangular prisms to rough material, formed with scales and agglomerates of different sizes, as can be observed in **Fig. S19B** of the support information.

Figs 7C-D show the EDS elemental chemical mapping of **1** before and after contact with ATV, respectively. Zn signals with a homogeneous distribution are observed in the as-synthesized **1**, as it expected for this compound (**Fig. 7C**). The presence of F and N signals in the EDS maps of **Fig. 7D** can be associated with the absorption of the ATV, which is evenly distributed along all the MOF structure. From this analysis is evident that the Zn-LMOF-based sensor interacts homogeneously with the ATV inducing a change in the morphology of the original material. To

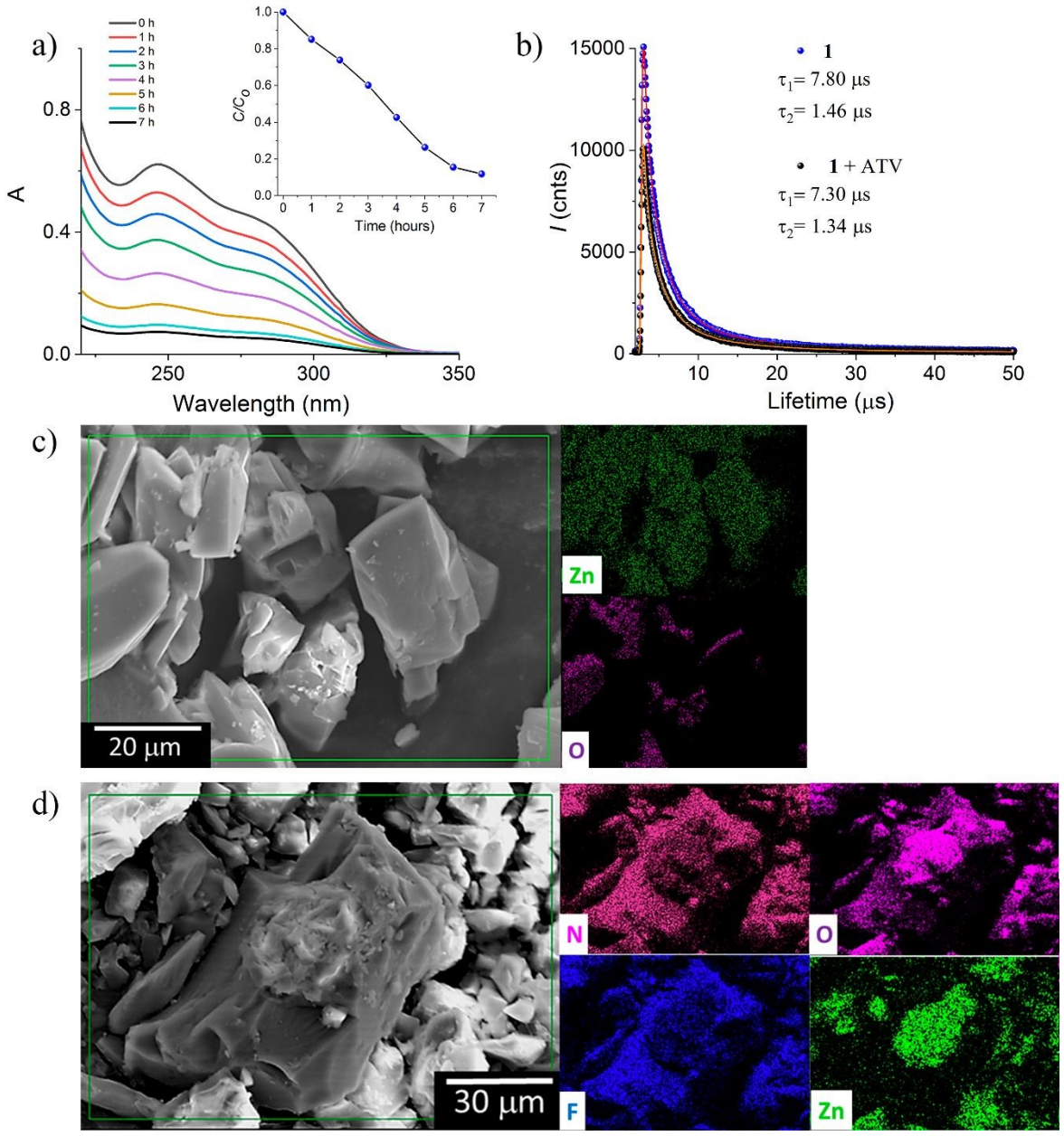

Fig. 7. a) Temporal evolution of UV-Vis spectra of ATV in the presence of crystals of **1** in ethanol. Inset: concentration changes of ATV in ethanol with increasing time. b) Fluorescence decay profiles of **1** in neutral ethanol-water dispersion before and after the addition of ATV (λ_{ex}= 354 nm). c) SEM images of the as-synthesized **1**. d) **1** treated with ATV showing EDS mapping elements O and Zn before and O, Zn, F and N signals after the contact with ATV solution.

View Article Online
DOI: 10.1039/D2TC00291D

ARTICLE

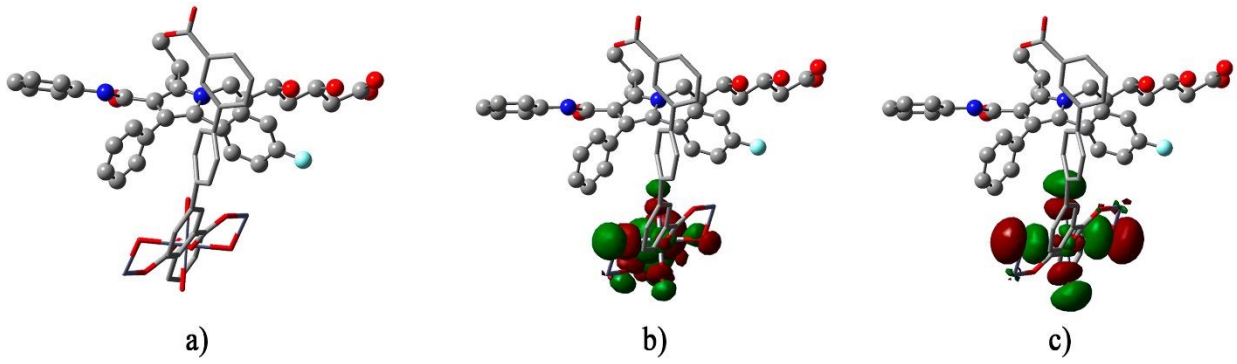

Fig. 8. a) Interacting fragments for all calculations (ATV *ball&stick style*; **1** section *tube style*), isosurfaces for frontier orbitals: b) HOMO and c) LUMO.

gain further insight into the interaction mode and selectivity of **1** towards ATV, density functional theory calculations were carried out using the Gaussian 16 suite programs[78] at the CAM-B3LYP/cc-pVDZ level of theory with a simulated solvent (acetonitrile) under the SMD continuum model.

The interaction energy, Eint, was calculated with the NBO Deletion (NBODel) formalism using the NBO3.1 program[79] as provided within the aforementioned suite.

A representative section of the MOF that includes the asymmetric unit of the crystal (**Fig. S20**) was selected to calculate their interaction with the analyte. The hydrogen atoms of the **1** section were optimized at the DFT level of theory mentioned above and the analyte was docked onto it manually and later was fully optimized at the same DFT level to allow for the analyte to freely move around the MOF section.

4-fluorophenyl and phenyl rings substituted at positions 2 and 3 of the pyrrole moiety respectively (see **Fig. 1** for the numbering of the structure) interact strongly with the central phenyl ring of terphenyl ligand from **1** section.

A large interaction energy of 111.04 kcal/mol between atorvastatin and the selected portion of the MOF as shown in **Fig. 8A**, was obtained with the NBODel method.

However, given the fact that both HOMO and LUMO reside on the Zn carboxylate moiety of the MOF section, this large value stems mainly from electrostatic interactions π-type stacking between the aromatic rings (**Fig. 8B-C**).

It is known that aromatic rings with electron deficiency have a strong luminous quenching ability when are bound to LMOFs through a photoinduced electron transfer (PET) process.[8081]

Thus, a static-complexation PET mechanism possibly in both the excited and the ground state could explain the efficient quenching process of **1** by ATV. Finally, the HOMO-LUMO gap for the interacting fragments was estimated with a value of 3.2 eV.

3. Conclusions

In conclusion, we have reported for the first time the selective and sensitive aqueous-phase detection of atorvastatin using MOF-based system. The porous nature, hydrolytic stability, and luminescent properties of Zn-MOF, **1** based on the π-electron-rich terphenyl-3,3″,5,5″-tetracarboxylic acid ligand have been utilized for designing a chemosensor that selectively detects atorvastatin at the micromolar concentration range in aqueous media at pH= 7.0.

Under these conditions, the addition of atorvastatin calcium exhibits a rapid and high luminescence quenching effect (K_{SV}= 1.402 x 10^5 M^{-1}) without the interference by other common anions such as dicarboxylates, oxyanions, and ATP, even in the presence of coexisting species in plasma and urine. The detection limit was estimated to be 4.21 μM.

Based on the crystal structure of **1**, spectroscopic titrations, lifetime measurements, SEM-EDS analysis, and DFT calculations the quenching process can be explained by a π-stacking PET-static quenching possibly in both the excited and the ground state.

Moreover, the Zn-MOF **1** can be used as an efficient luminescent sensor for the practical detection of atorvastatin in commercial pharmaceutical tablets.

Overall, these results highlight further the utility of luminescent metal-organic frameworks for sensing globally used drugs with potential application in real samples.

4. Experimental section

General Considerations. Chemicals, solvents, and instrumentations are listed in the Supporting Information. Synthesis of $\{[Zn_3(tptc)_2]\cdot(H_2O)_{1.3}\cdot(CH_3CH_2OH)_{3.1}\}_n$, 1. A mixture of [1,1′:4′,1″]terphenyl-3,3″,5,5″-tetracarboxylic acid (50mg, 0.123mmol) and $Zn(OTf)_2$ (89.46 mg, 0.246 mmol) in DMF:H_2O:EtOH (10:2:2 ml) was put into a 25 mL Teflon-lined stainless steel reactor. The reaction mixture was heated at 110°C for 24 h, and slowly cooled to room temperature. The

View Article Online
DOI: 10.1039/D2TC00284D

crystalline product of **1** was separated out by filtration, washed thoroughly with DMF/Ethanol and dried in vacuum at room temperature. Colorless crystals were obtained in 78% yield based on $Zn(OTf)_2$.

Anal. Calcd for $\{[Zn_3(Htptc)_2]\cdot(H_2O)_{1.3}\cdot(CH_3CH_2OH)_{3.1}\}_n$, **1** $C_{50.21}H_{43.24}O_{20.41}Zn_3$ C, 51.57; H, 3.72; N, 0.0. Found: C: 51.38; H, 3.85, N, 0.0.

Crystallographic investigations. The crystallographic data and refinement details for **1** are summarized in **Table S1**. Selected bond lengths and angles for **1** are listed in **Table S2**. Data were collected on a Bruker APEX II CCD diffractometer at 100 K; using Mo-K_α radiation (k = 0.71073 Å) from an Incoatec ImuS source and a Helios optic monochromator.[82] Suitable crystals were coated with hydrocarbon oil, picked up with a nylon loop, and mounted in the cold nitrogen stream of the diffractometer.

The structures were solved using intrinsic phasing (SHELXT) and refined by full-matrix least- squares on F2 using the ShelXle GUI.[83-84] The hydrogen atoms of the C–H bonds were placed in idealized positions.

The compound **1** crystalized as non-merohedral twin with 2 domains and BASF parameter 0.14517, the hklf4 format file was used to do the solventless refinement and use the ZQUEEZE/PLATON tool while the file with hlkf5 format was used to refine the proportion of solvent inside the crystal obtaining 3.10 of ethanol, 1.30 of water per unit of $C_{44}H_{22}O_{16}Zn_3$ as well as to obtain the proportion of the two domains of the twin.

CCDC 2116896 contains the supplementary crystallographic data for this paper. These data can be obtained free of charge from The Cambridge Crystallographic Data Centre via www.ccdc. cam.ac.uk/data request/cif.

Luminescence measurements. Luminescence spectra for solid-state and aqueous dispersions of **1** were recorded on an Agilent Cary Eclipse spectrophotometer equipped with a crystal-holder and a cell thermostated holder with a quartz cuvette, respectively. The as-synthesized **1** was dispersed (1 $mgmL^{-1}$) into a mixture ethanol/ double distilled water (v/v 8/2), and this mixture was stirring for 20 min at 25 °C. Fluorimetric titration experiments were carried out by adding aliquots of stock solutions of statins (10 mM) to the buffered ethanol/water (v/v, 8/2) dispersions of **1** (20 µM, pH = 7.0, 10 mM MOPS). After the addition of statins, the dispersion was equilibrated for 3 min before recording the emission spectrum (λ_{ex}= 330 nm) using a quartz cuvette. Luminescence quantum yields were determined using an aqueous solution of quinine sulfate containing H_2SO_4 (0.5 M) as a standard (Φ = 0.546; excited at 360 nm). For the determination of the quantum yield, the excitation wavelength was chosen so that A < 0.05.[70]

Fluorescence Lifetime Measurements. A custom-built Fluorescence Lifetime Imaging Microscope system was used to acquire the fluorescence lifetimes. A 354 nm picosecond laser pulsed at 10 MHz (LDH-P-FA-355, PicoQuant) was focused with a 0.40 NA reflective objective (LMM-40X-UVV-160, ThorLabs) into a 1.0 cm quartz cell containing the dispersion of **1** or directly on the crystalline sample in case of measurements in solid-state. The epifluorescence passed through a 425 nm long-pass dichroic mirror (Chroma T425lpxr-UF2), a 405 nm notch filter (Chroma ZET405nf), a 425 nm long pass emission filter (Chroma ET425lp) and was focused to single photon avalanche photodiode (PD-050-CTE, MPD). The laser controller (PDL-800-D, PicoQuant) and the detector were connected to a TCSPC card (PicoHarp 300, PicoQuant). The intensity of irradiation was set to obtain less than 1% of detection events. Back-scattered light from a mirror was used to obtain the IRF under the same conditions of irradiation. All data were obtained and treated in SymphoTime 64 software (PicoQuant). The lifetime data were fitted by bi-exponential decay functions.

SEM-EDS. Morphological changes of **1** before and after the contact with ethanolic solution of atorvastatin calcium were evaluated by Scanning Electron Microscopy (SEM) on a JSM-6510LV microscope from JEOL using the secondary electron detector. For sample preparation, the specimen was dried under room conditions and fixed on aluminum stubs with conductive double-stick tape and then coated with gold under vacuum using a Denton IV sputtering chamber. Elemental chemical distribution analysis was performed with an energy-dispersive X-ray spectroscope QUANTAX 200 from Bruker attached to SEM.

Author information

Corresponding Author *A. D.-G. tel: +52-55-56224514, e-mail: adg@unam.mx

†Supplementary Information:

Crystallographic data, IR and ^{13}C CPMAS NMR spectra, TGA plots, powder XRD data, SEM images and luminescent measurements.

Conflicts of interest

"There are no conflicts to declare"

Acknowledgements

We thank Chem. María A. Peña González, Ph. D Adriana Romo Perez, Ph. D Beatriz Quiroz-García, and M. Sc. Elizabeth Huerta Salazar for technical assistance. We thank PAPIIT-UNAM-216220 for financial support. L. D. R.-V and J. V.-G. are grateful to CONACyT for scholarships 713164 and 848787, respectively.

Notes and references

1 Recent Reviews 1-8
2 1 J. Dong, D. Zhao, Y. Lu and W. Y. Sun, J. Mater. Chem. A, 2019, **7**, 22744–22767.
3 2 M. O'Keeffe and O. M. Yaghi, Chem. Rev., 2012, **112**, 675–702.
4 3 M. D. Allendorf, C. A. Bauer, R. K. Bhakta and R. J. T. Houk, Chem. Soc. Rev, 2009, **38**, 1330–1352.
5 4 P. Raja Lakshmi, P. Nanjan, S. Kannan and S. Shanmugaraju, Coord. Chem. Rev., 2021, **435**, 213793.

6 5 L. E. Kreno, K. Leong, O. K. Farha, M. Allendorf, R. P. Van Duyne and J. T. Hupp, Chem. Rev., 2012, **112**, 1105–1125.
7 6 J. Heine and K. Müller-Buschbaum, Chem. Soc. Rev., 2013, **42**, 9232–9242.
8 7 Y. Liu, X. Y. Xie, C. Cheng, Z. S. Shao and H. S. Wang, J. Mater. Chem. C, 2019, **7**, 10743–10763.
9 8 M. Huangfu, M. Wang, C. Lin, J. Wang and P. Wu, Dalt. Trans., 2021, **50**, 3429–3449.
10 9 H. Deng, S. Grunder, K. E. Cordova, C. Valente, H. Furukawa, M. Hmadeh, F. Gándara, A. C. Whalley, Z. Liu, S. Asahina, H. Kazumori, M. O'Keeffe, O. Terasaki, J. F. Stoddart and O. M. Yaghi, Science, 2012, **336**, 1018–1023.
11 10 X. Zhang, W. Wang, Z. Hu, G. Wang and K. Uvdal, Coord. Chem. Rev., 2015, **284**, 206–235.
12 11 Y. Cui, Y. Yue, G. Qian and B. Chen, Chem. Rev., 2012, **112**, 1126–1162.
13 12 H. Wu, M. Li, C. Sun, X. Wang and Z. Su, Dalt. Trans., 2020, **49**, 5087–5091.
14 13 N. Zhang, D. Zhang, J. Zhao and Z. Xia, Dalt. Trans., 2019, **48**, 6794–6799.
15 14 X. Y. Wan, F. L. Jiang, L. Chen, J. Pan, K. Zhou, K. Z. Su, J. D. Pang, G. X. Lyu and M. C. Hong, CrystEngComm, 2015, **17**, 3829–3837.
16 15 J. Li, S. Chen, L. Jiang, D. Wu and Y. Li, Inorg. Chem., 2019, **58**, 5410–5413.
17 16 L. Li, H. Xue, Y. Wang, P. Zhao, D. Zhu, M. Jiang and X. Zhao, ACS Appl. Mater. Interfaces, 2015, **7**, 25402–25412.
18 17 D. Asnaghi, R. Corso, P. Larpent, I. Bassanetti, A. Jouaiti, N. Kyritsakas, A. Comotti, P. Sozzani and M. W. Hosseini, Chem. Comm., 2017, **53**, 5740–5743.
19 18 X. Zhang, Z. Zhang, J. Boissonnault and S. M. Cohen, Chem. Comm., 2016, **52**, 8585–8588.
20 19 D. De, T. K. Pal, S. Neogi, S. Senthilkumar, D. Das, S. Sen Gupta and P. K. Bharadwaj, Chem. Eur. J., 2016, **22**, 3387–3396.
21 20 X. C. Lu, H. L. Wang, X. Wang, Q. Z. Li and L. Liao, J. Clust. Sci., 2019, **30**, 1673–1681.
22 21 R. Haldar, R. Matsuda, S. Kitagawa, S. J. George and T. K. Maji, Angew. Chemie - Int. Ed., 2014, **53**, 11772–11777.
23 22 Y. Shu, Q. Ye, T. Dai, Q. Xu and X. Hu, ACS Sensors, 2021, **6**, 641–658.
24 23 W. P. Lustig, S. Mukherjee, N. D. Rudd, A. V. Desai, J. Li and S. K. Ghosh, Chem. Soc. Rev., 2017, **46**, 3242–3285.
25 24 K. Müller-Buschbaum, F. Beuerle and C. Feldmann, Microporous Mesoporous Mater., 2014, **216**, 171–199.
26 25 M.-L. Hu, S. A. A. Razavi, M. Piroozzadeh and A. Morsali, **Inorg. Chem. Front.,** 2020,**7**, 1598-1632
27 26 M. Pamei and A. Puzari, Nano-Structures and Nano-Objects, 2019, **19**, 100364.
28 27 P. Kumar, K. H. Kim, V. Bansal, A. K. Paul and A. Deep, Microchem. J., 2016, **128**, 102–107.
29 28 B. Yan, J. Mat. Chem. C, 2019, **7**, 8155–8175.
30 29 Z. Xiao, Y. Wang, S. Zhang, W. Fan, X. Xin, X. Pan, L. Zhang and D. Sun, Cryst. Growth. Des., 2017, **17**, 4084–4089.
31 30 J. C. Jin, J. Wu, Y. X. He, B. H. Li, J. Q. Liu, R. Prasad, A. Kumar and S. R. Batten, CrystEngComm, 2017, **19**, 6464–6472.
32 31 E. Zhang, P. Ju, Z. Zhang, H. Yang, L. Tang, X. Hou, J. You and J. jiang Wang, Spectrochim. Acta, Part A, 2019, **222**, 117207.
33 32 R. X. Yao, X. Cui, X. X. Jia, F. Q. Zhang and X. M. Zhang, Inorg. Chem., 2016, **55**, 9270–9275.
34 33 X. Y. Wan, F. L. Jiang, C. P. Liu, K. Zhou, L. Chen, Y. L. Gai, Y. Yang and M. C. Hong, J. Mater. Chem. A, 2015, **3**, 22369–22376.
35 34 J. Liu, J. Wu, Z. Luo, B. Li, A. Singh and K. Abhinav, J. Coord. Chem., 2017, **70**, 3946–3958.
36 35 J. Yang, L. Zhang, X. Wang, R. Wang, F. Dai and D. Sun, RSC Adv., 2015, **5**, 62982–62988.
37 36 X. Xu, Y. Guo, X. Wang, W. Li, P. Qi, Z. Wang, X. Wang, S. Gunasekaran and Q. Wang, Sensors Actuators, B Chem., 2018, **260**, 339–345.
38 37 L. D. Rosales-Vázquez, A. Dorazco-González and V. Sánchez-Mendieta, Dalt. Trans., 2021, **50**, 4470–4485.
39 38 H. Sirén, J Pharmacol Clin Toxicol, 2017, **5**, 1092.
40 39 M. Patel and C. Kothari, TrAC - Trend Anal. Chem., 2017, **86**, 206–221.
41 40 R. M. Calderon, L. X. Cubeddu, R. B. Goldberg and E. R. Schiff, Mayo Clin Proc., 2010, **85**, 349–356.
42 41 L. Cai, Z. Zheng, X. Wang, L. Tang, L. Mai, G. He, H. Lei and S. Zhong, Anal. Methods, 2017, **9**, 1038–1045.
43 42 A. Tavousi, E. Ahmadi, L. Mohammadi-Behzad, V. Riahifar and F. Maghemi, Microchem. J., 2020, **158**, 105159.
44 43 T. A. Silva, H. Zanin, F. C. Vicentini, E. J. Corat and O. Fatibello-Filho, Sens. Act. B Chem., 2015, **218**, 51–59.
45 44 Z. Kamalzadeh and S. Shahrokhian, Bioelectrochemistry, 2014, **98**, 1–10.
46 45 S. Altinöz and B. Uyar, Anal. Methods, 2013, **5**, 5709–5716.
47 46 S. Mazurek and R. Szostak, J . Pharm. Biomed., 2009, **49**, 168–172.
48 47 J. J. M. Nasr, N. H. Al-Shaalan and S. M. Shalan, Spectrochim. Acta, Part A. 2020, **237**, 118332.
49 48 D. Skorda and C. G. Kontoyannis, Talanta, 2008, **74**, 1066–1070.
50 49 H. W. Darwish, S. A. Hassan, M. Y. Salem and B. A. El-Zeany, Spectrochim. Acta - Part A Mol. Biomol. Spectrosc., 2013, **104**, 70–76.
51 50 L. Nováková, D. Šatínský and P. Solich, TrAC - Trend Anal. Chem., 2008, **27**, 352–367.
52 51 S. N. Ortega, A. J. Santos-Neto and F. M. Lancas, Anal. Methods, 2017, **9**, 3039–3048.
53 52 V. Sree Janardhanan, R. Manavalan and K. Valliappan, Arab. J. Chem., 2016, **9**, S1378–S1387.
54 53 A. L. Assassi, C. E. Roy, P. Perovitch, J. Auzerie, T. Hamon and K. Gaudin, J. Chromatogr. A, 2015, **1380**, 104–111.
55 54 N. Sultana, M. S. Arayne, N. Shafi, F. A. Siddiqui and A. Hussain, Anal. Methods, 2010, **2**, 1571–1576.
56 55 X. S. Miao and C. D. Metcalfe, J. Chromatogr. A, 2003, **998**, 133–141.
57 56 R. O. Gunache (Roșca), A. V. Bounegru and C. Apetrei, Inventions, 2021, **6**, 57.
58 57 T. A. Silva, H. Zanin, F. C. Vicentini, E. J. Corat and O. Fatibello-Filho, Analyst, 2014, **139**, 2832–2841.
59 58 S. D. Bukkitgar, N. P. Shetti and R. M. Kulkarni, Sensors Actuators, B Chem., 2018, **255**, 1462–1470.
60 59 S. Ashour, M. Bahbouh and M. Khateeb, Spectrochim. Acta - Part A Mol. Biomol. Spectrosc., 2011, **78**, 913–917.
61 60 J. C. Abbar and S. T. Nandibewoor, Colloids Surfaces B Biointerfaces, 2013, **106**, 158–164.
62 61 J. Peng, H. Tian, Q. Du, X. Hui and H. He, Microchim. Acta, , 2018, **185**, 1-9.
63 62 J. M. Serrano-Becerra, S. Hernández-Ortega, D. Morales-Morales and J. Valdés-Martínez, CrystEngComm, 2009, **11**, 226–228.
64 63 V. A. Blatov, A. P. Shevchenko and D. M. Proserpio, Cryst. Growth. Des., 2014, **14**, 3576–3586.
65 64 A. L. Spek, Acta Crystallogr., Sect. D Struct. Biol., 2009, **65**, 148–155.
66 65 C. F. Macrae, I. J. Bruno, J. A. Chisholm, P. R. Edgington, P. McCabe, E. Pidcock, L. Rodriguez-Monge, R. Taylor, J. Van De Streek and P. A. Wood, J. Appl. Crystallogr., 2008, **41**, 466–470.
67 66 H. A. Habib, A. Hoffmann and C. Janiak, Dalt. Trans., 2009, 1742–1751.
68 67 H. C. Hoffmann, M. Debowski, P. Müller, S. Paasch, I. Senkovska, S. Kaskel and E. Brunner, Materials (Basel)., 2012, **5**, 2537–2572.

View Article Online
DOI: 10.1039/D2TC00291D

69 68 X. Wang, C. Qin, E. Wang, Y. Li, N. Hao, C. Hu and L. Xu, Inorg. Chem., 2004, **43**, 1850–6.
70 69 L. D. Rosales-Vázquez, J. Valdes-García, I. J. Bazany-Rodríguez, J. M. Germán-Acacio, D. Martínez-Otero, A. R. Vilchis-Néstor, R. Morales-Luckie, V. Sánchez-Mendieta and A. Dorazco-González, Dalt. Trans., 2019, **48**, 12407-12420.
71 70 J. Carlos Rendón-Balboa, L. Villanueva-Sánchez, L. David Rosales-Vázquez, J. Valdes-García, A. R. Vilchis-Nestor, D. Martínez-Otero, S. Martínez-Vargas and A. Dorazco-González, Inorg. Chim. Acta, 2018, **483**, 235–240.
72 71 M. K. Salomón-Flores, C. L. Hernández-Juárez, I. J. Bazany-Rodríguez, J. Barroso-Flores, D. Martínez-Otero, R. López-Arteaga, J. Valdés-Martínez and A. Dorazco-González, Sens. Act. B Chem., 2019, **281**, 462–470.
73 72 V. Amendola, L. Fabbrizzi and E. Monzani, Chem. Eur. J., 2004, **10**, 76–82.
74 73 O. Fazlolahzadeh, A. Rouhollahi and M. Hadi, Anal. Bioanal. Electrochem., 2016, **8**, 566–577.
75 74 B. Dogan-Topal, B. Uslu and A. S. Ozkan, Comb. Chem. High Throughput Screen., 2007, **10**, 571–582.
76 75 I. J. Bazany-Rodríguez, M. K. Salomón-Flores, J. M. Bautista-Renedo, N. González-Rivas and A. Dorazco-González, Inorg. Chem., 2020, **59**, 7739–7751.
77 76 L. L. Lv, J. Yang, H. M. Zhang, Y. Y. Liu and J. F. Ma, Inorg. Chem., 2015, **54**, 1744–1755.
78 77 J. R. Lakowicz, Principles of fluorescence spectroscopy, Plenum Press, New York, Second edi., 1999.
79 78 M. J. Frisch, G. W. Trucks, H. B. Schlegel, G. E. Scuseria, M. a. Robb, J. R. Cheeseman, G. Scalmani, V. Barone, G. a. Petersson, H. Nakatsuji, X. Li, M. Caricato, a. V. Marenich, J. Bloino, B. G. Janesko, R. Gomperts, B. Mennucci, H. P. Hratchian, J. V. Ortiz, a. F. Izmaylov, J. L. Sonnenberg, Williams, F. Ding, F. Lipparini, F. Egidi, J. Goings, B. Peng, A. Petrone, T. Henderson, D. Ranasinghe, V. G. Zakrzewski, J. Gao, N. Rega, G. Zheng, W. Liang, M. Hada, M. Ehara, K. Toyota, R. Fukuda, J. Hasegawa, M. Ishida, T. Nakajima, Y. Honda, O. Kitao, H. Nakai, T. Vreven, K. Throssell, J. a. Montgomery Jr., J. E. Peralta, F. Ogliaro, M. J. Bearpark, J. J. Heyd, E. N. Brothers, K. N. Kudin, V. N. Staroverov, T. a. Keith, R. Kobayashi, J. Normand, K. Raghavachari, a. P. Rendell, J. C. Burant, S. S. Iyengar, J. Tomasi, M. Cossi, J. M. Millam, M. Klene, C. Adamo, R. Cammi, J. W. Ochterski, R. L. Martin, K. Morokuma, O. Farkas, J. B. Foresman and D. J. Fox, 2016, Gaussian 16, Revision C.01, Gaussian, Inc., Wallingford CT, 2016.
80 79 NBO Version 3.1, E. D. Glendening, A. E. Reed, J. E. Carpenter, and F. Weinhold.
81 80 W. Liu, C. Chen, Z. Wu, Y. Pan, C. H. Ye, Z. Mu, X. Luo, W. Chen and W. Liu, ACS Sustain. Chem. Eng., 2020, **8**, 13497–13506.
82 81 A. P. de Silva, H. Q. N. Gunaratne, T. Gunnlaugsson, A. J. M. Huxley, C. P. McCoy, J. T. Rademacher and T. E. Rice, Chem. Rev., 1997, **97**, 1515–1566.
83 82 APEX 2 Softw. Suite. Bruker AXS Inc., Madison, Wisconsin, USA, 2004.
84 83 C. B. Hübschle, G. M. Sheldrick and B. Dittrich, J. Appl. Crystallogr., 2011, **44**, 1281–1284.
85 84 G.M. Sheldrick, SHELXL-97, Progr. Cryst. Struct. Refinement, Univ. Göttingen, Germany 1997.
86